Absolute Calibration of the Lyman-α Measurement Apparatus at DIII-D

F. M. Laggner,[1, a)] A. Bortolon,[1] A. M. Rosenthal,[2] T. M. Wilks,[2] J. W. Hughes,[2] C. Freeman,[1] T. Golfinopoulos,[2] A. Nagy,[1] D. Mauzey,[1] M. W. Shafer,[3] and the DIII-D team[b)]

[1)] *Princeton Plasma Physics Laboratory, Princeton, New Jersey 08543, United States of America*

[2)] *MIT Plasma Science and Fusion Center, Cambridge, Massachusetts 02139, United States of America*

[3)] *Oak Ridge National Laboratory, Oak Ridge, Tennessee 37831, United States of America*

(Dated: 22 February 2023)

The LLAMA (LLAMA is the Lyman-Alpha Measurement Apparatus) diagnostic was recently installed on the DIII-D tokamak (Rosenthal *et al.*[1]). LLAMA is a pinhole camera system, with narrow band Bragg mirror, bandpass interference filter and an AXUV photodiode detector array, which measures the Ly-α brightness in the toroidal direction on the inboard, high field side (HFS), and outboard, low field side (LFS). This contribution presents a setup and a procedure for an absolute calibration near the Ly-α line at 121.6 nm.

The LLAMA in-vacuum components are designed as a compact, transferable setup that can be mounted in an ex-situ vacuum enclosure that is equipped with an absolutely calibrated Ly-α source. The spectral purity and stability of the Ly-α source are characterized using a vacuum ultraviolet (VUV) spectrometer while the Ly-α source brightness is measured by a NIST-calibrated photodiode. The non-uniform nature of the Ly-α source emission was overcome by performing a calibration procedure that scans the Ly-α source position and employs a numerical optimization to determine the emission pattern. Nominal and measured calibration factors are determined and compared, showing agreement within their uncertainties. A first conversion of the measured signal obtained from DIII-D indicates that the Ly-α brightness on the HFS and LFS are on the order of $10^{20}\,\mathrm{Ph\,sr^{-1}\,m^{-2}\,s^{-1}}$. The established calibration setup and procedure will be regularly used to re-calibrate the LLAMA during DIII-D vents to monitor possible degradation of optical components and detectors.

PACS numbers: 52.55.Fa, 52.70.-m, 52.70.Kz
Keywords: tokamak, plasma edge, spectroscopy, neutral density, hydrogen plasma, Lyman-alpha line

[a)]Electronic mail: flaggner@pppl.gov

[b)]See the appendix of 'DIII-D research towards establishing the scientific basis for future fusion reactors' by C. C. Petty and the DIII-D Team 2019 Nucl. Fusion **59** 112002, `https://doi.org/10.1088/1741-4326/ab024a`

I. INTRODUCTION AND BACKGROUND

A pinhole camera system, the LLAMA (LLAMA is the Lyman-Alpha Measurement Apparatus) was developed and installed at the DIII-D tokamak to measure the Lyman-alpha line (Ly-α) brightness across the plasma boundary and to infer neutral deuterium density profiles and ionization rate[1]. The implementation of the LLAMA builds on experience from previous vacuum ultraviolet (VUV) measurements of the Ly-α line radiation[2,3], which use AXUV photodiode arrays with Ly-α filters. The LLAMA employs a Bragg mirror in combination with a Ly-α filter to reject parasitic carbon line radiation close to the Ly-α wavelength that originates from plasma impurities due to DIII-D's carbon walls. AXUV photodiode arrays are used as detectors. The lines of sight (LOS) are below the midplane, oriented tangentially in the toroidal direction so as to cover the inboard, high field side (HFS), and the outboard plasma edge region low field side (LFS), with 20 channels in each array[1]. Measurements in the VUV range are notoriously challenging, for the scarcity of optical components and detectors as well as the need for the instrumentation to be placed in-vacuum. However, Ly-α line radiation provides some key advantages compared to the much more common measurements of Balmer series that lie in the visible part of the spectrum. At Ly-α wavelengths there are much reduced reflections from carbon (C) plasma facing components (PFCs), which can become a substantial issue for visible spectroscopy depending on the LOS geometry and the radiation characteristics of the plasma[4]. Furthermore, fewer molecular contributions around the Ly-α line are expected in comparison to the Balmer-alpha line (Ba-α) line for typical DIII-D operation conditions. This gives low background pickup when using VUV filter spectroscopy, where the filter bandpass is typically wider than the nominal line width.

Quantitative measurements of the Ly-α intensity require an absolute calibration of the LLAMA diagnostic. Furthermore, it is known that the detector responsivity of AXUV detectors used in high temperature plasma diagnostics suffers significant degradation upon radiation exposure[5,6]. This is a strong motivation for a promptly available and repetitive calibration of the LLAMA diagnostic. Absolute calibration of VUV diagnostics requires vacuum conditions, which means that the LLAMA diagnostic cannot be calibrated when mounted to DIII-D. Moreover, either a properly calibrated VUV light source, e.g. a synchrotron light source[7], or in-situ spectral information is needed. The spectral information is

required to allow application of line branching, line intensity ratios[8–10] and Bremstrahlung continuum[11,12] calibration procedures. Since filter spectroscopy used in LLAMA does not conserve any spectral information, most of the previously introduced approaches are not feasible. Because of the need for frequent LLAMA calibrations, a different calibration procedure using a compact, commercially available VUV source was employed. This imposes challenges because few of these sources are commercially available and if so, their radiation volume is relatively small and anisotropic.

The following contribution introduces the developed calibration setup and outlines the calibration procedure. Section II introduces the LLAMA components and their spectral sensitivity as well as the signal processing. The nominal calibration factor is introduced in section III. To enable an absolute calibration onsite at DIII-D, a calibration vacuum enclosure was assembled and equipped with a Ly-α source (section IV). Section V provides a characterization of the Ly-α source spectra to optimize operation conditions with high signal measured by the LLAMA as well as high Ly-α fraction. Section VI introduces the procedure for the absolute calibration and presents the calibration measurements of the Ly-α purity of the LLAMA signals. Section VII presents a comparison of nominal and measured calibration factors as well as absolutely calibrated brightness profiles that were measured in DIII-D. Section VIII discusses drawbacks of the presented approach and concludes with an outlook towards potential improvement of the calibration procedure and regular usage for re-calibration and monitoring purposes.

II. LLAMA OPTICS SETUP AND SIGNAL PROCESSING

This section introduces the main components and features of the LLAMA that are relevant for the nominal and absolute calibration procedure. A full description of all components as well as computer-aided design (CAD) renderings can be found in Rosenthal *et al.*[1].

For a proper measurement of Ly-α, located at 121.6 nm, it is important to suppress radiation from other plasma species, which in DIII-D is largely associated with carbon from the graphite PFCs[13]. To that end, LLAMA combines a VUV Bragg mirror[14] and bandpass interference filter[15], which reduce contributions from CIII line emission at 117.6 nm to roughly 10 % of the responsivity at Ly-α. Figure 1 presents the overall system responsivity of the LLAMA as a function of wavelength (λ) and indicates the suppression of the CIII

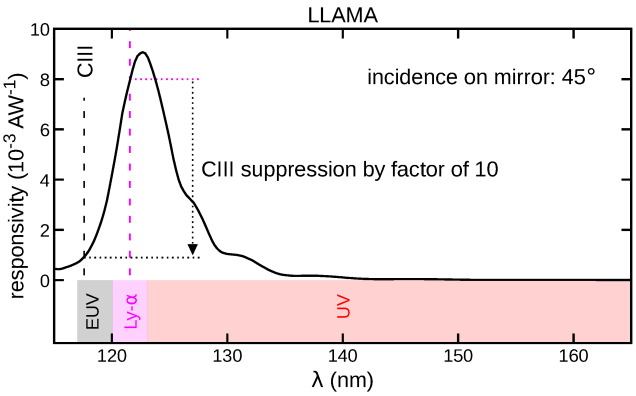

FIG. 1: Spectral responsivity of the LLAMA diagnostic: The LLAMA is designed to suppress a CIII line at 117.6 nm (as indicated by the dashed arrow) with maximum transmission around Ly-α (121.6 nm).

contributions. Here, the measured spectral responses of the Bragg mirror and the transmission filter are combined with the response of the AXUV photodiode detector, provided from the manufacturer data sheet[16], considering an angle of incidence (AOI) of 45° on the Bragg mirror. In the absolute calibration procedure the LLAMA spectral responsivity is considered to account for leakage from non-Ly-α spectral components of the Ly-α source (see section V C and figure 11).

The VUV Bragg mirror has a full width at half maximum (FWHM) of 5 nm around the Ly-α line. The Bragg reflectivity depends on the AOI and since the mirror is located less than 4 cm behind the pinhole, this leads to a variation of the AOIs for various channels as seen in figure 2. Figure 2a indicates that the peak reflectivity shifts towards higher λ for increasing AOI. This needs to be considered in the relative calibration from channel to channel since the AOI varies from 32° to 47° for the LFS views and from 48° to 56° for the HFS views. Figure 2b presents AOI distributions for the HFS and LFS views. The different distribution widths of both views are due to a roughly 15 % larger magnification on the LFS system at the tangency radius.

Under the typical Ly-α photon flux from DIII-D's plasma edge, the LLAMA's AXUV detectors are expected to generate photocurrents of the order of 1 nA to 100 nA. These are amplified by means of a set of low-noise transimpedance amplifiers[1], with configurable gains in the range of 10^7 V A^{-1} and 10^8 V A^{-1}, providing an output signal between 0.1 V and 10 V.

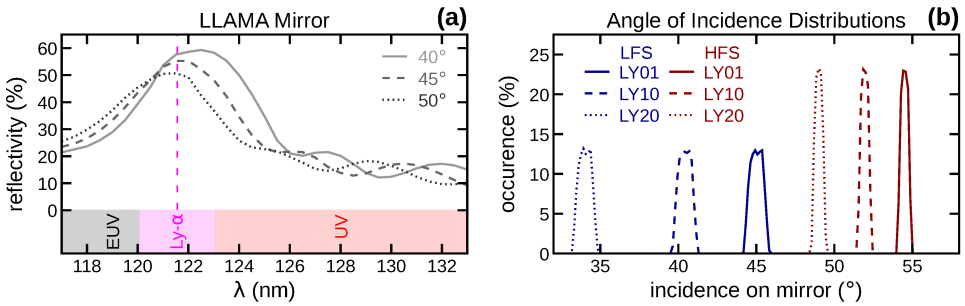

FIG. 2: Angular dependence of the LLAMA mirror reflectivity: (a) spectral reflectivity for different angle of incidence (AOI) and (b) AOI distributions of multiple LLAMA channels (LY01, LY10 and LY20). With increasing AOI the peak reflectivity shifts to higher wavelength (λ). The AOI distributions have a FWHM of 1.1° for the LFS channels and 0.6° at the HFS.

III. NOMINAL CALIBRATION OF LLAMA

The process of absolute calibration consists of determining for each LLAMA channel, ch, the coefficient, $C(ch)$, which provides the conversion from the measured signal of the LLAMA $S(ch)$ in V to a photon brightness $I(ch)$ in $\mathrm{Ph\,sr^{-1}\,m^{-2}\,s^{-1}}$:

$$I(ch) = C(ch) \cdot S(ch). \tag{1}$$

Nominal calibration factors $C_{\mathrm{nom}}(ch)$ can be determined using the nominal properties of the optical components, determined by spectral measurements or manufacturer specifications, and diagnostic geometry, determined by coordinate-measuring machine (CMM) metrology analysis:

$$C_{\mathrm{nom}}(ch) = \frac{1}{E(ch) \cdot R_{\mathrm{mir}}(ch) \cdot T_{\mathrm{fil}} \cdot G_{\mathrm{amp}}(ch) \cdot D_{\mathrm{det}}}, \tag{2}$$

where $E(ch)$ is the etendue, $R_{\mathrm{mir}}(ch)$ the mirror reflectivity, T_{fil} the filter transmissivity, $G_{\mathrm{amp}}(ch)$ the amplifier gain and D_{det} detector responsivity. The system's etendue is expressed by the $E(ch) = A_{\mathrm{pin}}/(d^2_{\mathrm{pin,det}}(ch)) \cdot A_{\mathrm{det}} \cdot \cos(\theta(ch))$, where A_{pin} is the area of the pinhole, $d_{\mathrm{pin,det}}(ch)$ is the distance from pinhole to detector pixel, A_{det} the detector pixel surface area and $\theta(ch)$ the angle of central ray incidence on the detector pixel.

Because of the dependence of R_{mir} on the AOI (see section II) and differences in viewing geometry of each detector pixel, $d_{\mathrm{pin,det}}$ and θ are expected to be the leading parameters responsible for the channel to channel variation of the calibration factors.

Of the quantities in equation (2), R_{mir}, T_{fil}, A_{det}, A_{pin} and G_{amp} are known from measurements of the components. These measurements were performed and provided from the component manufacturers. The geometrical parameters $d_{\mathrm{pin,det}}$, θ are inferred from CMM metrology analysis of the LLAMA assembly. Concerning the nominal detector response D_{det}, a nominal reference value of roughly $0.16\,\mathrm{A\,W^{-1}}$ at Ly-α is provided by the manufacturer. However, important deviations are reported in the literature, particularly in the Ly-α wavelength range[6,17], which effectively result in uncertainties of the order of 20 % on the nominal calibration factors (see section VI D, figure 14).

Inserting the nominal parameters in equation (2) yields $C_{\mathrm{nom}}(ch)$ on the order of $7 \pm 2 \cdot 10^{20}\,\mathrm{Ph\,sr^{-1}\,m^{-2}\,s^{-1}\,V^{-1}}$ for the HFS views and $2.1 \pm 0.5 \cdot 10^{20}\,\mathrm{Ph\,sr^{-1}\,m^{-2}\,s^{-1}\,V^{-1}}$ for the LFS views, with a channel to channel variation within 5 % (see also Section VI D, figure 14).

IV. LABORATORY VACUUM SETUP FOR ABSOLUTE CALIBRATION AT LY-α

While the nominal calibration can yield accurate quantitative measurements in the initial use of the diagnostic, a periodic photometric calibration is necessary to monitor and account for the potential detector degradation by radiation exposure. Because of the expectation that diagnostic calibrations need to be performed relatively frequently, promptly before and after DIII-D campaigns, on components that become activated over time, a calibration at an off-site synchrotron light source facility was deemed impractical. In-situ photometric calibration of the LLAMA diagnostic when installed on DIII-D was also not technically viable. A dedicated ex-vessel calibration apparatus was developed, providing vacuum conditions appropriate for VUV spectroscopy and equipped with a customized Ly-α source[18] by Resonance Ltd.

The Ly-α source is an electrodeless, sealed, radio frequency (RF)-excited gas discharge lamp with a magnesium fluoride window of 8 mm diameter. The emitting volume is contained in a cylindrical bulb with 9 mm diameter and 15 mm height. It operates with a helium-deuterium mixture, providing a full-spectrum nominal radiance of $5.0 \cdot 10^{15}\,\mathrm{Ph\,sr^{-1}\,s^{-1}}$ and a nominal Ly-α radiance of $5.0 \cdot 10^{13}\,\mathrm{Ph\,sr^{-1}\,s^{-1}}$. The source is installed in a shielded re-entrant arm. The lamp is powered by a small wall plug power supply and has a declared

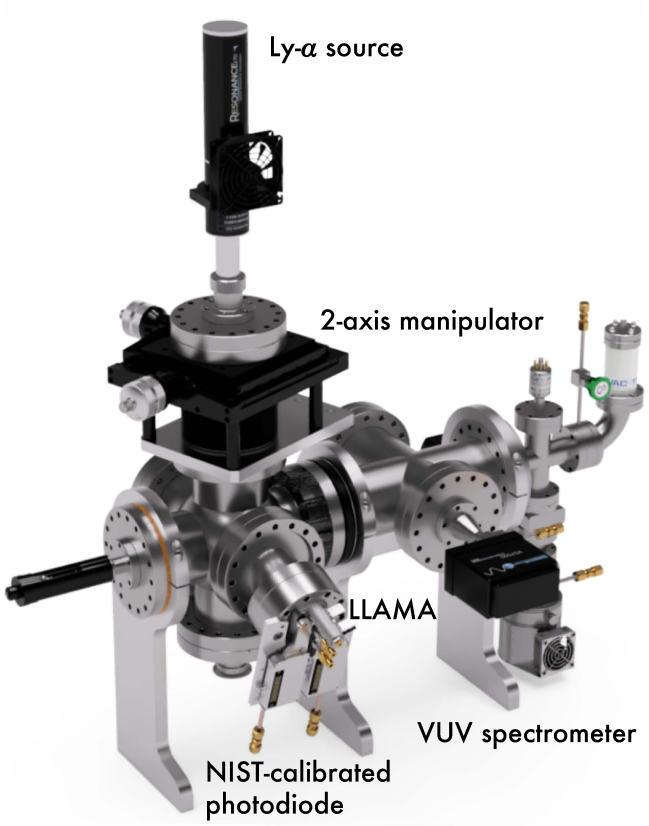

FIG. 3: CAD model of the LLAMA laboratory vacuum enclosure for calibration: The Ly-α source is inserted from the top into a 2-axis manipulator, looking down on the LLAMA, which is inserted via a customized adaptor, which re-creates the LOS geometry in DIII-D.

operating life often in excess of 4000 h. The Ly-α source is installed vertically on the dedicated ultra-high vacuum (UHV) enclosure, designed to optimize the optical coupling between the LLAMA and the Ly-α source (Figure 3). The UHV pumping system provides pressures of $2 \cdot 10^{-5}$ Pa, i.e. appropriate to avoid Ly-α absorption in residual gas. The calibration apparatus is located in laboratory space in the vicinity of DIII-D. Figure 4 presents a cutaway in the yz-plane through the vacuum enclosure and the HFS system of the LLAMA. The Ly-α source is inserted from the top into a 2-axis manipulator, enabling position adjustments in the xy-plane. The Ly-α source bulb is housed at the end of a re-entrant tube that is equipped with a 'quick disconnect adapter' vacuum feedthrough that allows for adjustment in the z-direction. This enables accurate positioning of the Ly-α source with respect to the LLAMA. Customized adapter flanges for the LFS and HFS views re-create the LOS geom-

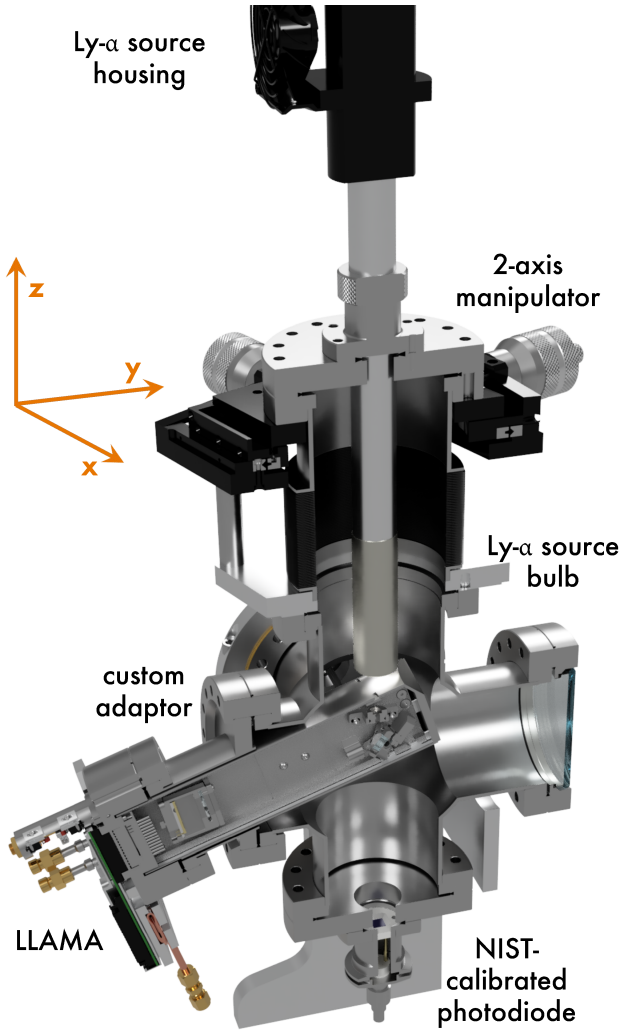

FIG. 4: Cutaway drawing of the LLAMA inserted into the calibration stand: The HFS pinhole is aligned to the re-entered bulb of the Ly-α source. The LLAMA in-vacuum components are the pinhole, the Bragg mirror and a detector box, housing the interference filter and AXUV detector array. Below the LLAMA a NIST-calibrated photodiode is located, allowing the re-calibration of the Ly-α source.

etry identical to the installed configuration inside the DIII-D vacuum vessel. The direction of the chief ray, launched from the detector center through the pinhole, is optimized to be aligned along the vertical z-axis.

To minimize electrical noise in the laboratory environment, the vacuum enclosure is insulated from the surrounding equipment and grounded to the reference potential of the measurement. During the absolute calibration procedure, the enclosure is connected to the potential of the amplifier system, which is also electrically isolated from any other LLAMA

components. The electrical insulation and common grounding of the amplifier circuits and the vacuum enclosure allow for a calibration measurement down to signal amplitudes in the range of 150 µV. This is partially enabled by the capability to modulate the Ly-α source, which allows for an effective offset subtraction (see V C), since the AXUV photodiodes used in LLAMA exhibit a dark current (also referred to as reverse bias leakage current) that gets amplified and causes an output signal offset.

Additionally, in order to monitor and track long term potential drifts of Ly-α source radiance, a NIST-calibrated photodiode[19] is installed below the LLAMA. For this procedure, the LLAMA is removed and the Ly-α source is fully inserted, illuminating directly NIST-calibrated photodiode and providing an absolute calibration of the Ly-α source source.

When necessary, the source can be relocated to a second flange, allowing direct LOS illumination of a compact Czerny-Turner VUV spectrometer[20] (VS7550 MINI), also depicted in figure 3. The VUV spectrometer allows characterization of the Ly-α source spectrum for varied source operation parameters (temperature and modulation), which is critical for optimizing Ly-α intensity measured by the LLAMA during the calibration (see section V). During spectral characterization, the source is fully inserted horizontally, so that the source aperture is at approximately 5 cm from and aligned with the spectrometer entrance slit.

It should be noted that, while the calibration apparatus allows an optimized illumination of the diagnostic, the dimensions of the Ly-α source are comparable with the rectangular LLAMA pinholes (8 mm height and 2 mm width). This entails an additional effort, compared to the extended source photometric calibration in the visible range, to accurately take into account the LOS geometry and source emissivity distribution.

V. SPECTRAL CHARACTERIZATION OF THE LY-α SOURCE AND LLAMA RESPONSE

For an accurate LLAMA calibration, it is important to evaluate the potential contribution of different spectral regions to the measured LLAMA signal. In fact, the latter includes strong molecular and atomic emission other than Ly-α, which could leak through the systems spectral bandpass and contribute to the measured LLAMA signal. This issue is particularly critical in view of the relatively small radiance delivered by the source at Ly-α, compared to Balmer series and molecular radiation. The spectral characterization is performed ex-

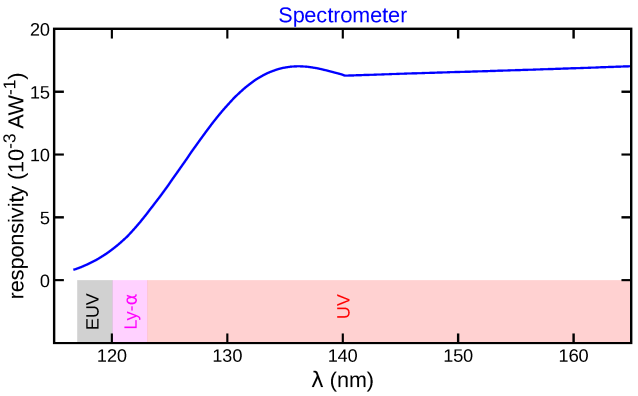

FIG. 5: Spectral responsivity of the VS7550 MINI spectrometer according to manufacturer specifications: Due to the MgF window the spectral sensitivity falls off towards the Ly-α.

ploiting two capabilities of the Ly-α source. First, the temperature of the internal source components can be adjusted, which changes the outgassing of deuterium (D) inside the lamp and consequently the gas pressure. This provides control on the relative intensities of the Ly-α line and the surrounding molecular bands, which can be optimized for the LLAMA calibration. Second, the Ly-α source light output can be modulated with a frequency of up to 1 kHz by switching the RF power supply, allowing for easier signal offset subtraction.

A. Temperature Dependence of the Source Spectrum

The Ly-α source spectrum was characterized using the compact VUV spectrometer introduced in the previous section. The VUV spectrometer was configured with a 1200 mm^{-1} grating, with a 25 µm entrance slit, for a λ resolution at the first order maximum of 0.45 nm. Figure 5 presents the spectral responsivity of the VUV spectrometer in this configuration as provided by manufacturer specifications, showing a steep decrease below 130 nm mainly associated with the spectral transmissivity of the spectrometer's magnesium fluoride window. This responsivity is accounted for when modeling the spectral response of the LLAMA to variations of the Ly-α source spectrum. This procedure is initiated with a pre-heating phase of roughly 20 min at elevated temperatures of 100 °C, which is used to achieve thermal equilibrium of the components surrounding the source, then the source temperature is stepped down to 55 °C. This is the lowest temperature at which Ly-α output is detected. After another 10 min equilibration phase, a step-wise scan of the source temperature is performed

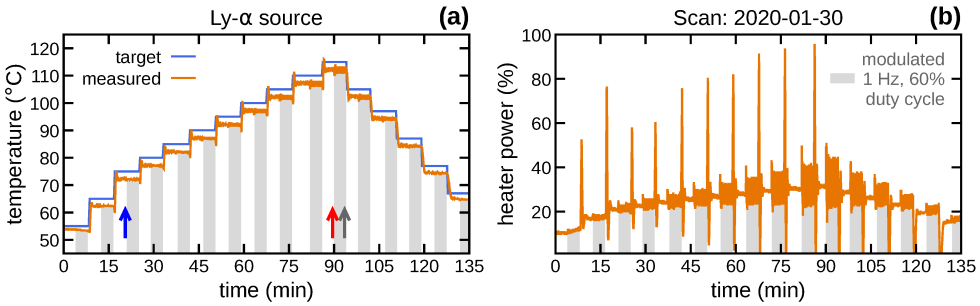

FIG. 6: Step-wise variation of the Ly-α source temperature: (a) Ly-α source target (blue) and measured (orange) temperatures and (b) Ly-α source heater power. The three vertical arrows indicate the times of three example spectra presented in figure 7. Each temperature step has two 4 min long phases with continuous and modulated operation.

as shown in figure 6. Each of the steps contains a 4 min phase where the source is operated continuously, followed by a 4 min phase with a square wave modulation with 1 Hz and 60 % duty cycle (gray shaded background). As seen in figure 6b the heater power, here shown as the percentage of the maximum applicable power, oscillates by up to 20 % in the modulation phase. This raised the question whether the spectral composition might change when the Ly-α source is modulated and motivated a detailed comparison of the Ly-α source spectra for different source temperatures as well as operational modes. During the last 30 s of each phase, a VUV spectrum is acquired. Three arrows in figure 6 indicate the times of three example spectra discussed in the following.

The relative amplitude of the different spectral components of the Ly-α source was observed to vary strongly with the operation temperature of the source itself. This effect can be illustrated by comparing spectra taken at 75 °C and 115 °C, which were compensated for the spectral responsivity of the VUV spectrometer (figure 5). Figure 7 compares spectra covering a range in λ larger than the spectral responsivity of the LLAMA (see figure 1). The colored arrows at the bottom of figure 6a indicate the corresponding times of the spectra shown in figure 7. The spectral range in figure 7a shows the Ly-α line, the surrounding Lyman band, 90 nm to 165 nm, and the less pronounced the Werner band, 90 nm to 130 nm, which both originate from molecular D. Moreover, a molecular radiation continuum is observed between 170 nm to 300 nm. More detailed studies on the radiation spectra of hydrogen (H) gas discharges have been carried out in the past[21–23] and good models for their description have been developed[24,25]. Typically the main parameters that determine the spectral

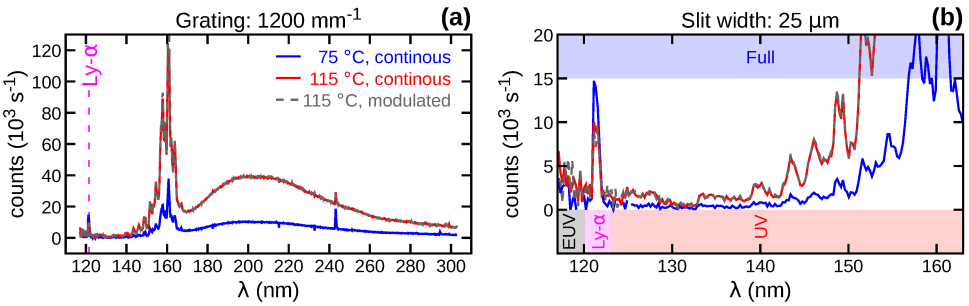

FIG. 7: Spectra of the Ly-α source for different operation temperatures: (a) full UV spectrum showing molecular lines and a continuum and (b) magnified VUV range at distinct operation temperatures. As the operation temperature is increased (see corresponding arrows on figure 6a), the molecular contributions go up and the Ly-α brightness decreases. The source modulation does not affect the spectrum when accounting for the duty cycle.

compositions of such discharges are the neutral gas pressure, injected RF power and the achieved plasma temperature. For the purpose of the LLAMA calibration procedure, it is important to have flexibility in tuning the Ly-α source temperature to vary the spectral contributions. A 50 % higher Ly-α intensity is observed at 75 °C in comparison to the spectrum measured at 115 °C (see figure 7b). Importantly, no difference is observed in the spectrum for continuous or modulated Ly-α source operation, as seen in the spectra taken at 115 °C.

B. Spectral sensitivity of LLAMA

To evaluate the potential contribution of different spectral regions to the measured LLAMA signal, it is useful to separate the spectra, recorded by the VUV spectrometer, into regions that are indicated by colored horizontal boxes in figure 7b.

The spectra recorded by the VUV spectrometer (compensated for the spectral responsivity) during the Ly-α source temperature scan (section V A) are convolved with the nominal LLAMA responsivity (figure 1) and the amplifier gain. This leads to a nominal output voltage dependence on the source temperature, for each component separately. Figure 8 compares these responses for the three parts of the Ly-α source spectrum, as indicated in figure 7b. While the 'Full' signal (blue) increases towards source temperatures of roughly 90 °C, it flattens out at larger temperatures. The 'Ly-α' contribution to the LLAMA signal

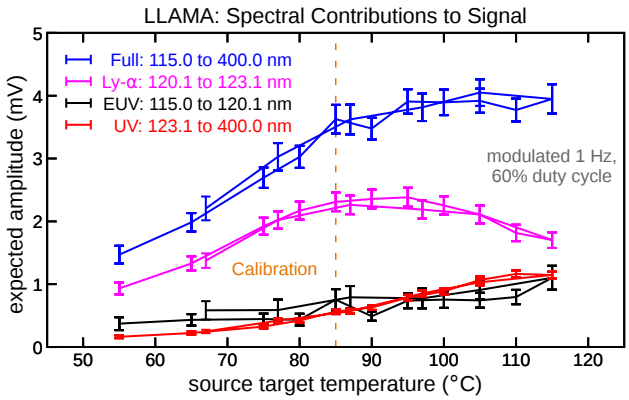

FIG. 8: Expected spectral contributions to the LLAMA signal to determine spectral leakage in the calibration process. The lines connect temporally sequenced data. A maximum of the Ly-α contribution is seen around 85 °C, the optimal source temperature for the calibration measurements as indicated by the vertical dashed line.

(magenta) rolls over between 80 °C and 100 °C. A maximum of the 'Ly-α' contribution is observed around 85 °C, the optimal source temperature for the calibration measurements (orange vertical dashed line). The contributions from the 'EUV' (black) and 'UV' (red) increase continuously towards higher temperatures, mainly because of an increasing baseline around the Ly-α line as seen in figure 7b. This baseline falls still into the responsivity window of the LLAMA and contributes to the 'Full' signal especially at higher source temperatures. It should be noted that figure 8 contains data from stepping up and stepping down the source temperature as indicated by the lines, which connect temporally sequenced points. This demonstrates that the Ly-α source spectra are reproducible and that the temperature steps are properly chosen, since no hysteresis occurs in these curves.

C. Expected and Measured spectral response of the LLAMA

To confirm the expected source temperature dependence of the LLAMA signal as shown in figure 8, a second source temperature scan was performed, where now the LLAMA is illuminated by the modulated Ly-α source (1 Hz modulation frequency with 60 % duty cycle). This allows comparing the expected response with the measured one, as well as determining the optimal source temperature to perform the absolute calibration.

This scan consists in a series of 10 s long LLAMA acquisitions at various source temper-

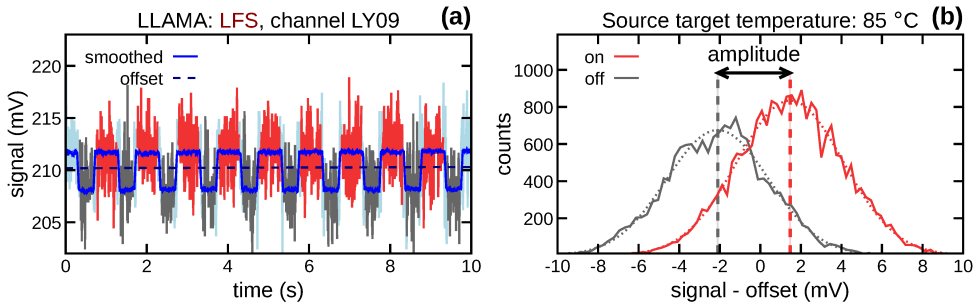

FIG. 9: Absolute calibration of the LLAMA: (a) Ly-α source signal recorded by LLAMA channel 9 during 1 Hz modulation and (b) Signal amplitude determined by Gaussian fits to the raw data for both 'on' (source light output) and 'off' (dark current offset) phases.

atures, with the analog output of all channels digitized with a 10 kHz digitizer. Figure 9a shows an example time trace of the recorded LLAMA signal of the LFS system channel 9. Raw-data as well as smoothed signal exhibit the modulation of the Ly-α source. From the smoothed signal, the 'on' and 'off' periods (red and gray) are identified in figure 9a, neglecting 50 ms windows around the switch. A linear offset subtraction (dashed line) accounts for potential drifts. The raw-data distributions of both periods allows the extraction of the signal amplitude as shown in figure 9b. Under the assumption of white noise, Gaussian distributions are fitted to the data recorded with the source modulated 'on' and 'off'. The difference of their position (vertical dashed lines) indicates the signal amplitude. Moreover, the fit uncertainties in the position of each Gaussian distribution (vertical shaded areas) can be propagated through the further calibration procedure. Tests indicated that this method produces reliable results down to signal amplitudes of roughly 150 µV. Figure 10 compares the LLAMA measurement (red) with the 'Full' spectral response as presented in figure 8 (blue). The latter is scaled to match the measurement at 85 °C. Both signals show the same trend over the range of varied source temperature, confirming the robustness of the modeled response of the system.

The relative weight of the spectral components shown in figure 8 can then be used to determine the fraction of the emission reaching the LLAMA detector during a calibration exposure, which is associated with pure Ly-alpha emission, at any given source temperature. This is formally represented by the quantity $F_{\mathrm{Ly}-\alpha}$:

$$F_{\mathrm{Ly}-\alpha} = \frac{S_{\mathrm{Ly}-\alpha}}{S_{\mathrm{full}}}. \tag{3}$$

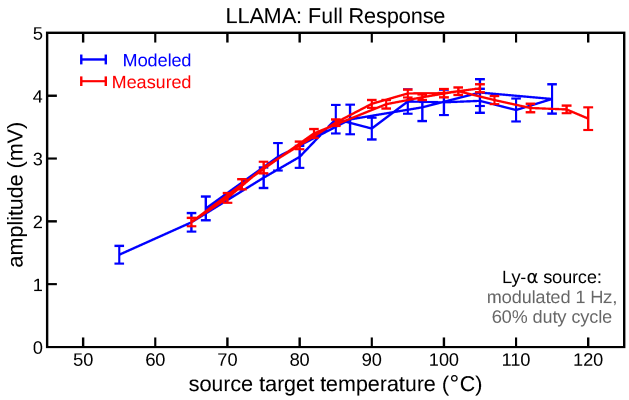

FIG. 10: Modeled and measured LLAMA signal: The modeled full spectrum response of the LLAMA signal amplitude (blue) is reproduced by measured actual LLAMA signal (red).

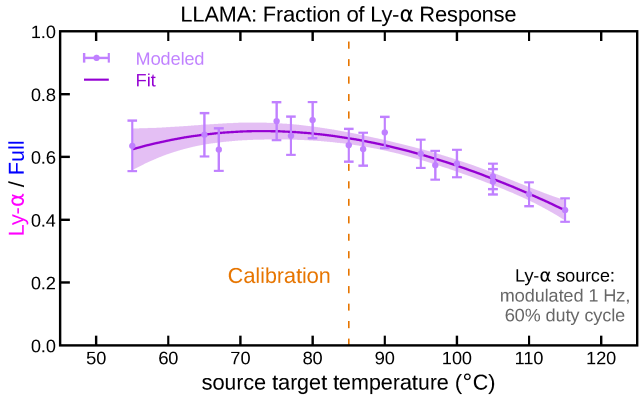

FIG. 11: Fraction of Ly-α in the LLAMA signal: As the source target temperature is increased, the fraction of Ly-α brightness rolls over. The orange dashed line indicates the temperature of the LLAMA calibration, combining a good $F_{\mathrm{Ly}-\alpha}$ and overall signal.

From the measured temperature dependence of $F_{\mathrm{Ly}-\alpha}$, the actual Ly-α contribution to the LLAMA signal in the calibration procedure is identified and properly accounted (see section V C). Figure 11 presents a spline fit with Monte Carlo uncertainties to the data of the ratio of the Ly-α line to the full spectrum, 'Ly-α/Full', which is $F_{\mathrm{Ly}-\alpha}$. The result indicates that over a broad range of operating temperatures, a non-negligible fraction (35 % to 55 %) of the LLAMA photocurrent is associated with leakage of non-Ly-α emission from the source.

VI. ABSOLUTE CALIBRATION OF THE LLAMA

This section describes in detail the LLAMA absolute calibration procedure, which is structured in three main parts:

1. Diagnostic alignment and Ly-α source preparation (section VI A)

2. Collection of the calibration data set (section VI B)

3. Modeling of measured Ly-α brightness (section VI C)

Section VI D compares the results of the absolute calibration procedure to the normal calibration factors.

A. Diagnostic alignment and source preparation

The calibration is performed sequentially for the LFS and HFS views. The first step is to install the LLAMA diagnostic, adjusting the alignment so that nominal direction of the chief ray of the selected view (e.g. LFS) is aligned with the direction of the Ly-α source, which is the vertical axis. This is accomplished with the help of an alignment tool, which can also be used to align the components on a horizontal optic table[1]. In this case the tool is mounted directly to the LLAMA flange. The LLAMA orientation is adjusted until it aligns with the vertical axis, within an accuracy of 1° to 2°. Once a satisfactory alignment is found, the vacuum enclosure is sealed and pumped down to $2 \cdot 10^{-5}$ Pa.

The source is turned on in modulated illumination mode with 1 s modulation period and 60 % duty cycle. The source is then brought to optimal temperature of 85 °C, illustrated for reference by a vertical orange dashed line in figure 8. At this temperature, the source provides the highest Ly-α fraction at the highest total LLAMA response, i.e. maximizing signal to noise ratio while minimizing non-Ly-α components. The apparatus is ready for collecting the calibration data set.

B. Collection of the calibration data set

When the LLAMA pinhole is illuminated by the modulated Ly-α source, the Ly-α source position in the horizontal plane is adjusted using the 2-axis manipulator, and measurements

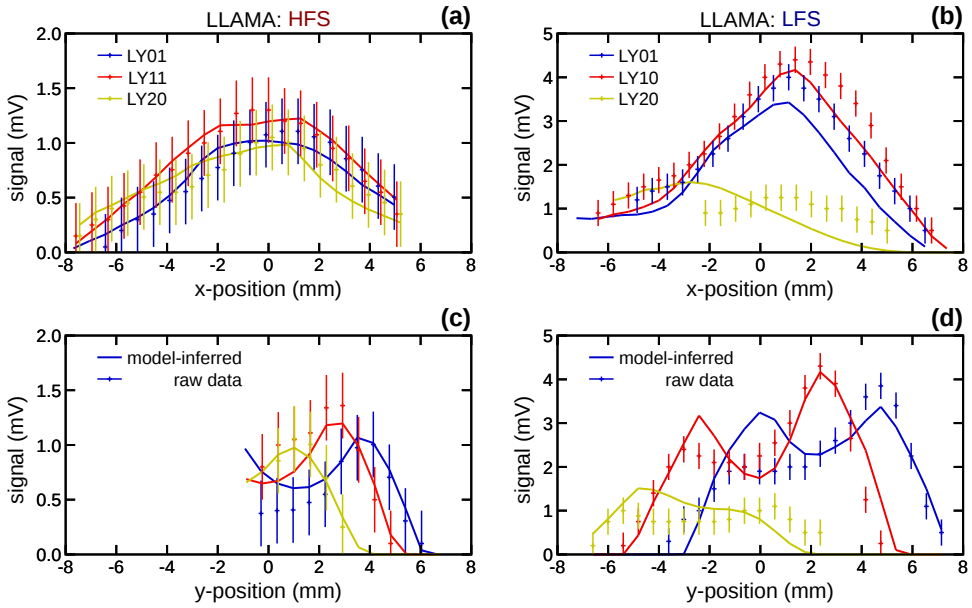

FIG. 12: 2-axis manipulator position scans measured for the (a,c) HFS and of the (b,d) LFS system: The data is plotted against the source position measured in direction perpendicular (x-position) and parallel (y-position) to the detector array in the plane of the Ly-α source. The inferred model is consistent for the LFS and HFS, showing agreement on HFS system and agreement on the peak values of the LFS system.

are taken at selected x-y locations, so as to provide a y-scan at fixed x, and an x-scan at fixed y. This is necessary because the Ly-α source does not fully fill the viewing cone of the AXUV detector pixels and even more important the Ly-α source radiance is non-uniform. In other words, the LLAMA calibration measurements determine $S(ch)$ for various positions of the 2-axis manipulator as well as channels. For the first LLAMA calibration, approximately 30 sampling points in the xy-plane were collected for the HFS as well as LFS system. Figure 12 presents these measurements for three channels ('raw data') as well as the optimized model ('model-inferred'), that will be introduced in section VI C. These scans provide a data set sufficient for the absolute calibration. Once completed, the procedure is repeated for the other view (HFS).

C. Modeling of measured Ly-α brightness

Photometric calibrations in the visible range typically rely on calibration spheres, or Lambertian plates which approximate a uniform and isotropic source, allowing the solution

of equation (1) directly. However, this approach is not applicable to the Ly-α source used for this calibration because the Ly-α source size is comparable to the size of the diagnostic collection cones. For instance the LOS into the source vary for different channels and have a directional sampling of smaller sub-volumes of the Ly-α source. These effects are amplified in view of the acquired data (section VI B, figure 12) suggesting that the emissivity distribution inside the source is non-uniform. As a result, the solution of equation (1) requires an accounting for the full geometry of the illumination configuration as well as the 3D emissivity distribution inside the source volume. To accomplish this task numerically, a multi-parameter model was developed, which implements a Monte Carlo (MC) approach to compute the Ly-α brightness during a Ly-α source exposure of the LLAMA.

Formally, the measured signal $S(ch)$ is related to the source and detector characteristics via the following equation:

$$S(ch) = \frac{1}{C_{\mathrm{src}}(ch)} \cdot \frac{1}{F_{\mathrm{Ly}-\alpha}} \cdot \sum_{i=1}^{\mathrm{n}} \int_0^{L_i(ch)} \epsilon(r,\phi,z)\mathrm{d}l. \tag{4}$$

Here, $C_{\mathrm{src}}(ch)$ represents the calibration factor obtained by this procedure, ϵ the source emissivity distribution and $F_{Ly-\alpha}$ the Ly-α fraction factor, because only a fraction (section V C, figure 11) of the spectrum contributes to the measured signal. If ϵ was well known, the equation could be directly solved by a MC process, launching n MC rays (n = 2000) along randomized optical paths from the AXUV detector pixel through the pinhole into the source volume. From the line integral of the Ly-α source emissivity along their path $L(ch)$, the nominal brightness (photon flux towards the detector) could be computed. However, at the time of this work the detailed measurements or reconstructions of the source emissivity distribution ϵ were not available. For this reason, an approach was applied that expresses ϵ as a function of a small set of parameters, which are then adjusted to optimize the match between the extended set of calibration measurements and the corresponding simulated signal reconstructions. Specifically, guided by the observation of hollowed profiles in figure 12, ϵ is assumed to be inhomogeneous inside the cylindrical source bulb of radius a_{src} and height h_{src} and described by the following parametric expression:

$$\epsilon(r,\phi,z) \approx \epsilon(r,z) = P_{\mathrm{cal}} \cdot \left[o + \left(\frac{r}{a_{\mathrm{src}}}\right)^v \cdot \frac{1}{w\sqrt{2\pi}} e^{-\frac{1}{2}(\frac{z-h/2}{w})^2}\right]. \tag{5}$$

In the model the spatial distribution of the emissivity is described by three parameters:

1. o represents a constant emissivity background

2. v describes a hollow emission feature in radial direction

3. w determines the localization of the hollow emission feature along the bulb axis

P_{cal} is a normalization factor adjusted to ensure that the simulated radiance matches the nominal source radiance. In practice, for given set of v, w and o, P_{cal} is adjusted so that the Ly-α photon flux of $1.15 \cdot 10^{12}\,\mathrm{Ph\,s^{-1}}$ from the NIST-calibrated photodiode measurement is matched.

Additionally, to account for inaccuracies of the relative orientation of the LLAMA and the Ly-α source during 2-axis manipulator position scans (directions indicated in figure 4), six additional parameters are included in the optimization process. These are the source position offset in x and y direction (x_{offs}, y_{offs}), the tilt against xy-plane in x and y direction (x_{tilt}, y_{tilt}), the rotation of 2-axis manipulator axis against x- and y-direction (m_{tilt}) and the source to pinhole distance ($d_{\mathrm{sour,pinh}}$). Finally, to facilitate the optimization and obtain a robust solution, the number of free parameters is reduced by expressing the calibration factors as:

$$C_{\mathrm{src}}(ch) = B \cdot C_{\mathrm{nom}}(ch). \tag{6}$$

This simplification is equivalent to assuming that the variation in the diagnostic response is not channel dependent, reducing the problem to finding a single scaling factor B for each measured LLAMA view (HFS or LFS view) that represents the average scaling of the diagnostic response compared to the nominal response. This assumption is justified considering that the primary causes of response degradation are aging of the optical components and detector, which occurs by irradiation, by penetrating radiation and/or thermal cycles during baking procedures. In the numerical approach employed, the parameter scaling factor B is also considered as an additional optimization parameter. All in all, equation (4) is solved by optimizing up to ten parameters using a non-linear χ^2-minimization to fit the experimental data. The result of the optimization yield best fit estimates of B, and therefore C_{src} from equation (6), as well as the emissivity distribution of the source and the source-diagnostic geometrical configuration. The covariance matrix of the minimization process can be used to estimate the uncertainties on the optimized parameters.

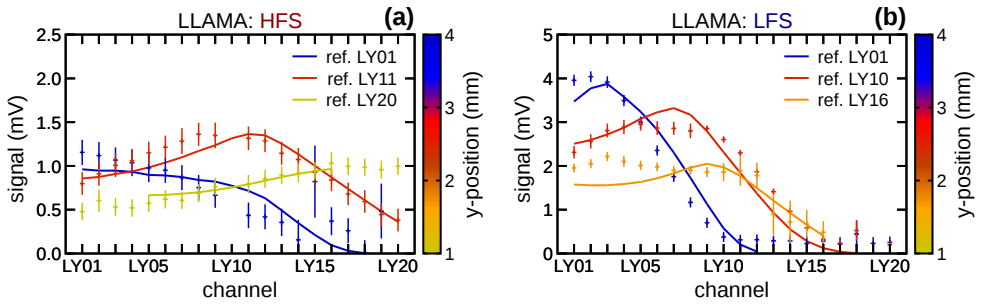

FIG. 13: Calibration measurements for three different 2-axis manipulator locations across all LLAMA channels for (a) HFS and for (b) LFS systems: The signals of neighboring channels only vary within the expected changes from the inferred model, pointing to no major variations of the calibration factor of individual channels.

D. Absolute calibration results

The optimization procedure was applied 'globally' to the full calibration data set, including measurements taken from both x- and y-scans of the manipulator, during exposures of both the LFS and the HFS system. In this minimization the three parameters describing ϵ (see equation (5)) are constrained to be the same for HFS and LFS systems.

Figure 13 compares calibration measurements across the 20 channels of the HFS and LFS systems (points) taken at three different source positions with modeled measurements obtained from equation (4) (lines) using the optimized set of parameters. Satisfactory agreement is found for both views and all source positions, indicating that, within the measurement uncertainties, the model assumptions are appropriate to capture the relevant features of the calibration setup. This is true in particular with regard to the three-parameter description of source emissivity, and the simplifying assumption of unique degradation scaling factor B for all the channels of a system. The key results of the optimization procedure are summarized in table I. For both the LFS and HFS systems the scaling factors B close to unity are found, indicating that the response of both systems are consistent with the nominal performance of the diagnostic apparatus. This is consistent with expectations, since the calibration was performed after assembly and prior to installation on the tokamak, i.e. before exposure to deteriorating agents. Concerning the source emissivity distribution ϵ, the results in table I indicate that the data set is consistent with a hollow emissivity distribution, with the emission localized radially near the bulb wall ($o \approx 0$, $v \approx 5$), varying weakly along

parameter	HFS	LFS
B	1.09 ± 0.10	1.01 ± 0.10
v	5.2 ± 1.6	5.2 ± 1.6
w	$500 \pm 100\,\mathrm{mm}$	$500 \pm 100\,\mathrm{mm}$
o	0.0 ± 0.1	0.0 ± 0.1
$d_{\mathrm{sour,pinh}}$	$19.3 \pm 2.0\,\mathrm{mm}$	$26.3 \pm 1.4\,\mathrm{mm}$

TABLE I: : Optimized parameters for calibration model

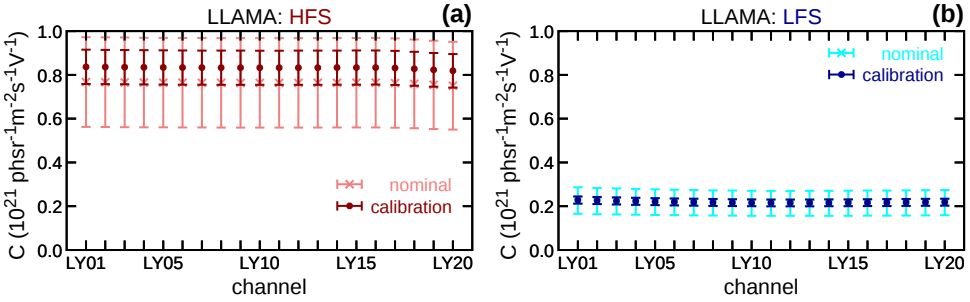

FIG. 14: Calibration factors (C) for the (a) HFS and for the (b) LFS systems of the LLAMA. The calibration procedure results in similar C as the estimation of the nominal calculation.

the bulb axis ($w \approx 500\,\mathrm{mm}$). As anticipated, geometrical configuration parameters can be included in the optimization to compensate for the lack of accurate spatial measurements. In this case, for instance, the distance between the source window and the LLAMA pinholes, which can not be measured inside the vacuum enclosure, could be inferred to a 2 mm accuracy (table I).

Figure 14 compares the calibration factors C_{src} obtained from equation (6) with the nominal calibration factors C_{nom}, showing good agreement within the respective uncertainties. As discussed in section III, the uncertainties of C_{nom} largely result from the uncertainty in the detector responsivity at Ly-α, whereas the uncertainties of C_{src} are computed from the covariance matrix of the optimization problem. It is important to note that the calibration results and their uncertainties formally depend on the model parameters. Nevertheless, the measured C_{src} results in uncertainties of 10 %, comparable or smaller than the nominal calibration and appropriate to discern and track potential degradation of the optical

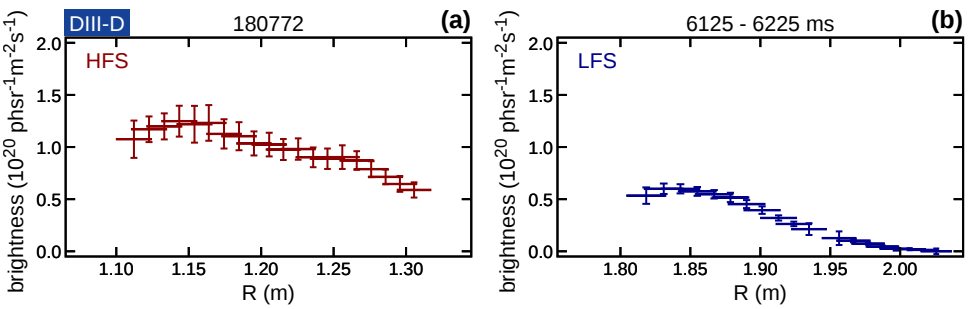

FIG. 15: Absolutely calibrated brightness profile of a LLAMA measurement in DIII-D (a) on the HFS and (b) on the LFS.

elements.

VII. ABSOLUTELY CALIBRATED LY-α MEASUREMENTS

With the outputs of the calibration measurements, C_{src} allows for Ly-α brightness profile measurements at DIII-D. Figure 15 presents a conversion of the signals measured inside DIII-D to radial brightness profiles of a inner wall limited, ohmic plasma discharge with a major plasma radius of 1.67 m, a toroidal magnetic field of 1.7 T, a plasma current of 1 MA and core line averaged electron density of $2.8 \cdot 10^{19}\,\mathrm{m}^{-3}$. Here, the measured brightness of individual channels are shown as a function of the tangency radius of their light collection cone and the signal from the outermost channel of the LFS system has been used as an offset reference. A detailed description of the LLAMA LOS geometry can be found in Rosenthal *et al.*[1]. The plasma boundary is located around 1.17 m on the HFS and 1.92 m on the LFS, so that in this configuration the views cover the region from the confined plasma and the scrape-off layer (SOL), where the emission from excited D neutrals is expected. The observed Ly-α brightness is on the order of $10^{20}\,\mathrm{Ph\,m^{-2}\,sr^{-1}\,s^{-1}}$, which is consistent with the expected values, for neutral densities of $10^{14}\,\mathrm{m}^{-3}$ to $10^{16}\,\mathrm{m}^{-3}$ and typical edge plasma parameters. Note that the finite brightness measured by the innermost channels of the LFS and HFS system is a result of the line integration across the outer plasma layers. Local Ly-α emissivity can be inferred through Abel inversion of the line integrated brightness measurements.

VIII. DISCUSSION AND OUTLOOK

This contribution presented a calibration setup and procedure to absolutely calibrate the LLAMA diagnostic at DIII-D, using a small footprint, commercially available Ly-α source. The process requires transferring of the LLAMA diagnostic to a dedicated calibration vacuum enclosure. For the LLAMA diagnostic, the impact of this transfer is mitigated by having two identical assemblies of the diagnostic, which can be swapped periodically avoiding interruption of diagnostic support. This allows frequent calibrations needed to monitor and track potential deterioration of the optical components, in particular the AXUV photodiode detectors.

As for all commercially available VUV sources, the Ly-α source used here is non-uniform and non-isotropic, which makes it impossible to apply methodologies typical for photometric calibrations in the visible range. To overcome this critical issue, the calibration procedure relies on parametric modeling of the geometry of the calibration setup as well as the emissivity distribution inside the Ly-α source. The derived measured calibration factor is close to the nominal calibration factor, confirming that the method delivers the appropriate accuracy.

One limitation of the approach presented is that it does not account for channel to channel variations of C_{src} beyond the expected variations of C_{nom}. This results from the need to reduce the number of free parameters in the model optimization to a reasonably tractable problem. While this was a convenient simplification for this first demonstration, it is by no means a general limitation of the approach. Indeed, a better knowledge of the source emissivity coupled with judicious choice of illumination data set, can provide sufficient constraints to extend the calibration to all channels separately.

Near term efforts will focus on measuring the emissivity distribution inside the Ly-α source, using a dedicated Si-diode detector equipped with a 2 mm diameter pinhole collimator, and leveraging the source maneuverability of the calibration apparatus. With the Ly-α source emissivity characterized in detail, it is expected that it will become feasible to determine calibration factors between individual LLAMA channels.

ACKNOWLEDGMENTS

This material is based upon work supported by the U.S. Department of Energy, Office of Science, Office of Fusion Energy Sciences, using the DIII-D National Fusion Facility, a DOE Office of Science user facility, under Awards DE-AC02-09CH11466, DE-AC05-00OR22725, DE-FC02-04ER54698 and DE-SC0014264.

DISCLAIMER

This report was prepared as an account of work sponsored by an agency of the United States Government. Neither the United States Government nor any agency thereof, nor any of their employees, makes any warranty, express or implied, or assumes any legal liability or responsibility for the accuracy, completeness, or usefulness of any information, apparatus, product, or process disclosed, or represents that its use would not infringe privately owned rights. Reference herein to any specific commercial product, process, or service by trade name, trademark, manufacturer, or otherwise, does not necessarily constitute or imply its endorsement, recommendation, or favoring by the United States Government or any agency thereof. The views and opinions of authors expressed herein do not necessarily state or reflect those of the United States Government or any agency thereof.

DATA ACCESS

The data that support the findings of this study are available from the corresponding author upon reasonable request.

REFERENCES

[1]A. M. Rosenthal, J. W. Hughes, A. Bortolon, F. M. Laggner, T. M. Wilks, R. Vieira, R. Leccacorvi, E. Marmar, A. Nagy, C. Freeman, and D. Mauzey, submitted to Review of Scientific Instruments (2020).

[2]R. L. Boivin, J. W. Hughes, B. LaBombard, D. Mossessian, and J. L. Terry, Review of Scientific Instruments **72**, 961 (2001).

[3]A. W. Degeling, H. Weisen, A. Zabolotsky, B. P. Duval, R. A. Pitts, M. Wischmeier, P. Lavanchy, P. Marmillod, and G. Pochon, Review of Scientific Instruments **75**, 4139 (2004).

[4]E. M. Hollmann, A. Y. Pigarov, and R. P. Doerner, Review of Scientific Instruments **74**, 3984 (2003).

[5]P. Kuschnerus, H. Rabus, M. Richter, F. Scholze, L. Werner, and G. Ulm, Metrologia **35**, 355 (1998).

[6]M. Bernert, T. Eich, A. Burckhart, J. C. Fuchs, L. Giannone, A. Kallenbach, R. M. McDermott, B. Sieglin, and Asdex Upgrade Team, Rev Sci Instrum **85**, 033503 (2014).

[7]R. D. Wood and S. L. Allen, Review of Scientific Instruments **59**, 1537 (1988).

[8]A. Greiche, W. Biel, O. Marchuk, and R. Burhenn, Review of Scientific Instruments **79**, 093504 (2008).

[9]K. D. Lawson, I. H. Coffey, J. Zacks, M. F. Stamp, and J.-E. contributors, Journal of Instrumentation **4**, P04013 (2009).

[10]L. Zhang, S. Morita, Z. Xu, Z. Wu, P. Zhang, C. Wu, W. Gao, T. Ohishi, M. Goto, J. Shen, Y. Chen, X. Liu, Y. Wang, C. Dong, H. Zhang, X. Huang, X. Gong, L. Hu, J. Chen, X. Zhang, B. Wan, and J. Li, Review of Scientific Instruments **86**, 123509 (2015).

[11]C. Dong, S. Morita, M. Goto, and H. Zhou, Review of Scientific Instruments **81**, 033107 (2010).

[12]J. M. Muñoz Burgos, K. Tritz, D. Stutman, R. E. Bell, B. P. LeBlanc, and S. A. Sabbagh, Physics of Plasmas **22**, 123301 (2015).

[13]P. M. Anderson, C. B. Baxi, E. E. Reis, J. P. Smith, and P. D. Smith, Fusion Engineering and Design **9**, 9 (1989).

[14]See `https://www.actonoptics.com/products/excimer-laser-optics` for further information on the deployed Bragg mirror.

[15]See `https://www.actonoptics.com/products/filters-narrowband` for further information on the deployed band-bass interference filter.

[16]See `https://optodiode.com/pdf/AXUV20ELGDS.pdf` for further information on the deployed AXUV photodiode detector array.

[17]C. Benson, G. D. Orebi Gann, and V. Gehman, The European Physical Journal C **78**, 329 (2018).

[18]See http://resonance.on.ca/line-source-hhelm-l-2/ for further information on the Ly-α source.

[19]See https://mcphersoninc.com/detectors/vuv-si-diode.html for further information on the NIST-calibrated photodiode.

[20]See http://resonance.on.ca/vs7550-uv-mini-spectrometer/ for further information on the VS7550 MINI VUV spectrometer.

[21]D. Wagner, B. Dikmen, and H. F. Döbele, Review of Scientific Instruments **67**, 1800 (1996).

[22]J. Komppula and O. Tarvainen, Plasma Sources Science and Technology **24**, 045008 (2015).

[23]U. Fantz, S. Briefi, D. Rauner, and D. Wünderlich, Plasma Sources Science and Technology **25**, 045006 (2016).

[24]D. Wünderlich, S. Dietrich, and U. Fantz, Journal of Quantitative Spectroscopy and Radiative Transfer **110**, 62 (2009).

[25]D. Wünderlich and U. Fantz, Atoms **4**, 26 (2016).